

XSPLAIN: XAI-enabling Splat-based Prototype Learning for Attribute-aware INterpretability

Dominik Galus¹ **Julia Farganus**¹ **Tymoteusz Zapala**¹ **Mikołaj Czachorowski**¹ **Piotr Borycki**²
Przemysław Spurek^{2,3} **Piotr Syga**¹

Abstract

3D Gaussian Splatting (3DGS) has rapidly become a standard for high-fidelity 3D reconstruction, yet its adoption in multiple critical domains is hindered by the lack of interpretability of the generation models as well as classification of the Splats. While explainability methods exist for other 3D representations, like point clouds, they typically rely on ambiguous saliency maps that fail to capture the volumetric coherence of Gaussian primitives. We introduce XSPLAIN, the first ante-hoc, prototype-based interpretability framework designed specifically for 3DGS classification. Our approach leverages a voxel-aggregated PointNet backbone and a novel, invertible orthogonal transformation that disentangles feature channels for interpretability while strictly preserving the original decision boundaries. Explanations are grounded in representative training examples, enabling intuitive “this looks like that” reasoning without any degradation in classification performance. A rigorous user study (N=51) demonstrates a decisive preference for our approach: participants selected XSPLAIN explanations 48.4% of the time as the best, significantly outperforming baselines ($p < 0.001$), showing that XSPLAIN provides transparency and user trust.¹

1. Introduction

Recent years have observed an accretion of deep learning methods dedicated to 3D due to growing data acquisition, mainly in fields such as robotic applications (Keetha et al., 2024), autonomous driving (Zhou et al., 2024), augmented reality and medical imaging (Li et al., 2024). Although they achieve impressive performance, their decision-making

¹Wrocław University of Science and Technology ²Jagiellonian University ³IDEAS Research Institute. Correspondence to: D. Galus <279690@student.pwr.edu.pl>.

Preprint. February 12, 2026.

¹The source code for this work is available at: [GitHub](https://github.com/DominikGalus/XSPLAIN).

processes remain largely unclear or rely on spurious correlations (Buhrmester et al., 2021). To overcome these limitations, a class of solutions has been proposed under the umbrella of eXplainable AI (XAI) (Xu et al., 2019) to provide transparency and interpretability. Generally, these algorithms are grouped into two categories: post-hoc approaches and ante-hoc approaches, where the model is designed to be interpretable by nature. Post-hoc methods serve pre-trained models without altering their architecture, such as SHAP (Lundberg & Lee, 2017), LIME (Ribeiro et al., 2016), LRP (Bach et al., 2015), and Grad-CAM (Selvaraju et al., 2020). However, they usually focus on a single instance and provide saliency maps that may not provide decisive insights. Ante-hoc models incorporate interpretable architectures and usually use *prototypes* (Chen et al., 2019; Nauta et al., 2023; Struski et al., 2024), which are beneficial for explaining a given phenomenon by relating it to the dataset used to train the model. Although significant progress has been made in explaining 2D image classifiers, explainability in 3D remains considerably less explored, despite the increasing adoption of 3D representations in real-world systems.

Recently, 3D Gaussian Splatting (3DGS) (Kerbl et al., 2023) has emerged as a powerful representation for modeling complex geometry, offering an efficient and continuous alternative to point clouds and meshes (Bao et al., 2025; Chen & Wang, 2025). Although 3DGS has been extensively studied in the context of rendering and reconstruction, its use for discriminative tasks such as classification (Zhang et al., 2025a) and, more importantly, the interpretability of such models, has received limited attention. Existing explanation methods for 3D data often rely on point-level saliency or gradient-based attribution, which can be noisy, difficult to interpret, and do not leverage the spatial coherence inherent in Gaussian-based representations.

In this work, we address these limitations by introducing **XSPLAIN**, an ante-hoc, prototype-based explainable framework for the classification of objects represented by 3D Gaussian primitives. Our XSPLAIN can operate as a standalone classifier, as the interpretability mechanism is a plug-in module that does not influence classification performance. Our method produces explanations that are both *faithful* to

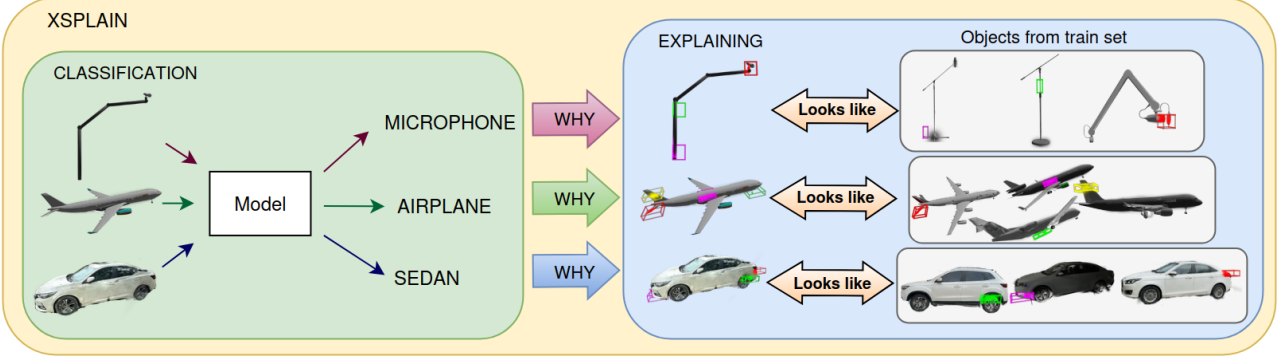


Figure 1. XSPLAIN provides ante-hoc, prototype-based explanations for 3D Gaussian Splat classification. A PointNet-based classifier predicts the object category from Gaussian Splat representations, while identifying the most influential voxel regions that drive the decision. Explanations are generated by retrieving representative training examples that activate similar latent responses in the same regions, enabling intuitive “looks like that” reasoning grounded in both geometry and semantic attributes.

the model’s decision process and *interpretable* to humans by establishing the predictions in spatially localized and semantically consistent regions of the 3D representation.

At a high level, XSPLAIN builds on a PointNet-inspired (Charles et al., 2017) backbone with a voxel aggregation module that preserves spatial structure while remaining permutation-invariant. The model is trained in two stages: first, the backbone is optimized purely for classification, second, the trained backbone is frozen, and a learnable, invertible transformation is optimized to disentangle feature channels for interpretability while strictly preserving the original decision boundaries. Building on this disentangled representation, XSPLAIN employs a prototype-based interpretability mechanism. For each feature channel, representative training examples are identified and used as prototypes, allowing explanations to be formed by direct comparison between regions of the test sample and analogous regions in the training data. Explanations are thus expressed as localized subsets of Gaussian primitives, offering intuitive, example-based insights into the model’s predictions.

We evaluate XSPLAIN on multiple 3D Gaussian Splatting classification benchmarks, focusing on subsets of the Shape-Splat (Ma et al., 2024) dataset and the MVImageNet-GS (Zhang et al., 2025a) benchmark. Our experiments demonstrate that XSPLAIN maintains competitive classification performance while producing coherent, spatially grounded explanations. Qualitative results show that the identified regions correspond to meaningful object parts, while quantitative analyzes validate the disentanglement and stability of the learned representations.

In summary, our contributions are threefold:

- We introduce the first ante-hoc, prototype-based explainability method for classification models operating on 3D Gaussian Splatting representations.

- We propose a PointNet-inspired architecture and a stage-wise feature disentanglement strategy guided by a purity objective, enabling spatially coherent, semantically isolated explanations.
- We conduct a comprehensive evaluation on multiple 3D Gaussian Splatting datasets, comparing XSPLAIN against existing post-hoc explainability methods and demonstrating improved interpretability while maintaining competitive classification performance.

2. Related Work

Prototype-based explainability In safety-critical applications, explanations are required to verify that decisions are grounded in meaningful characteristics rather than spurious cues. While some methods examine models post-hoc (Crabbé et al., 2021), intrinsic (ante-hoc) interpretability (Koh et al., 2020) aims to build transparent models from scratch. Prototype learning for deep neural networks usually involves finding structures in latent space representations. ProtoPNet (Chen et al., 2019) introduces learnable prototypes for each class in the spirit of ‘this looks like that’ reasoning, which agrees with human perception, where the final prediction is a weighted sum of prototype scores. As prototypes usually exhibit similarity, ProtoPShare (Rymarczyk et al., 2021) introduces a merge-pruning mechanism to merge redundant prototypes, improving stability and prediction accuracy. Other extensions focus on utilizing classifiers other than linear ones, like the decision tree in ProtoTree (Nauta et al., 2020) or KNN in ProtoKNN (Ukai et al., 2023). The applicability of prototypes extends beyond images, covering motion analysis (ProtoFormer; Han et al., 2024) or tabular data (ProtoGate; Jiang et al., 2024). Deformable ProtoPNet (Donnelly et al., 2022) and TesNet (Wang et al., 2021) introduce orthogonality constraints to further enhance prototypes flexibility and transparency. InfoDisent (Struski

et al., 2024) is a hybrid approach utilizing a trainable orthogonal transformation on pixel space to enable disentanglement of feature space, thus associating each channel with a prototype. EPIC (Borycki et al., 2025) introduces post-hoc feature channel disentanglement to find representative patches for the most active channels in the sample.

Point Cloud Interpretability Intrinsic methods introduce specific architecture design, like XPCC (Arnold et al., 2023) with prototype based classifier that utilizes kernel point CNN to extract features and class-weighted similarity to representative prototypes for the final decision, Interpretable3D (Feng et al., 2024) that optimizes prototypes based on the cosine similarity to the correct predictions or C-PointNet (Zhang et al., 2019) which modifies the former architecture by replacing the max pooling layer with a class-attentive feature module, assigning each point to the class that maximizes the activation value. InfoCons (Li et al., 2025) applies information-theoretic approach to extract a group of interpretable critical concepts. On the other hand, post-hoc methods are usually model-agnostic, like LIME3D (Tan & Kotthaus, 2022) that explains a point cloud by fitting a surrogate model on a perturbed original sample, Feature Based Interpretability introduced in (Levi & Gilboa, 2024) that evaluates per-point contribution based on pre-bottleneck features’ probing, or BubblEX (Matrone et al., 2022) that introduces interpretability module based on GradCAM to generate saliency maps conditioned on a class. PointMask (Taghanaki et al., 2020) incorporates a differentiable masking layer to mask out points with negligible contribution. They also show that PointNet architecture is prone to learn from bias pattern in training dataset.

Gaussian Splatting Interpretability 3DisGS (Zhang et al., 2025b) proposes a generative framework for single-view reconstruction with feature disentanglement at both coarse and fine-grained levels, such that each dimension encodes an interpretable semantic factor. However, it is an unsupervised approach with an image input, without clear relevance to the classification on pure 3D objects presented in this work.

3. XSPLAIN

Our framework consists of 3 components: (1) a backbone network inspired by PointNet (Charles et al., 2017) with a voxel aggregation module, (2) a trainable parametrized matrix for feature disentanglement, and (3) a prototype-based interpretability mechanism. Crucially, our approach follows a two-stage training procedure: the backbone is trained for classification, then frozen, while the parametrized matrix is optimized for interpretability. The architecture and the explaining procedure are illustrated in Fig. 2.

Problem Formulation Let $\mathcal{G} = \{g_i\}_{i=1}^N$ denote a 3D Gaussian Splatting representation with N Gaussian prim-

itives. We consider only geometric attributes, excluding view-dependent color:

$$g_i = (\mathbf{x}_i, \mathbf{s}_i, \mathbf{q}_i, \alpha_i) \in (\mathbb{R}^3, \mathbb{R}^3, \mathbb{R}^4, \mathbb{R}^1), \quad (1)$$

where \mathbf{x}_i denotes the 3D position, \mathbf{s}_i the anisotropic scaling factors, \mathbf{q}_i the orientation quaternion, and α_i the opacity. This choice is motivated by recent findings (Zhang et al., 2025a) showing that geometric attributes alone encode rich structural semantics, while excluding color improves robustness to appearance variations and reduces input dimensionality. This formulation allows our method to generalize to scenarios where color information may be unavailable or unreliable, e.g., objects reconstructed under varying illumination or from depth sensors.

Backbone architecture Our backbone is based on the PointNet architecture (Charles et al., 2017). We employ two Spatial Transformer Networks for input alignment: one operating in 3D coordinate space and another in the 64-dimensional feature space-followed by shared 1D convolutions that produce per-point feature vectors $\mathbf{f}_i \in \mathbb{R}^C$. The key modification we introduce is a **voxel aggregation module** that replaces the global max-pooling operation, providing spatial structure for interpretability while improving robustness to outliers.

Voxel Aggregation Module To establish a spatially structured representation suitable for interpretability, we employ an **intrinsic partitioning strategy**. Specifically, we partition the normalized input space into a regular grid of G^3 voxels. Crucially, the voxel index $v(i)$ for each Gaussian primitive is assigned *prior* to the Spatial Transformer Network based on its initial coordinates:

$$v(i) = \lfloor \tilde{x}_i \cdot G \rfloor \cdot G^2 + \lfloor \tilde{y}_i \cdot G \rfloor \cdot G + \lfloor \tilde{z}_i \cdot G \rfloor, \quad (2)$$

where coordinates are clipped to $[0, G - 1]$. This design choice ensures that explanations are anchored in the object’s original coordinate frame rather than a learned canonical pose. As a result, the spatial attribution directly reflects where the model attends in the input space, providing transparent insight into positional dependencies of the classifier.

This index $v(i)$ serves as immutable metadata bound to each primitive throughout the network. Point features are subsequently aggregated within each voxel using max-pooling:

$$\mathbf{h}_v = \max_{i:v(i)=v} \mathbf{f}_i \in \mathbb{R}^C. \quad (3)$$

Structure Preservation via Decoupling This architectural choice decouples local feature aggregation from global semantic integration. Unlike standard PointNet (Charles et al., 2017) which collapses all spatial information via global max-pooling, our voxel strategy preserves the association between features and their coarse spatial locations.

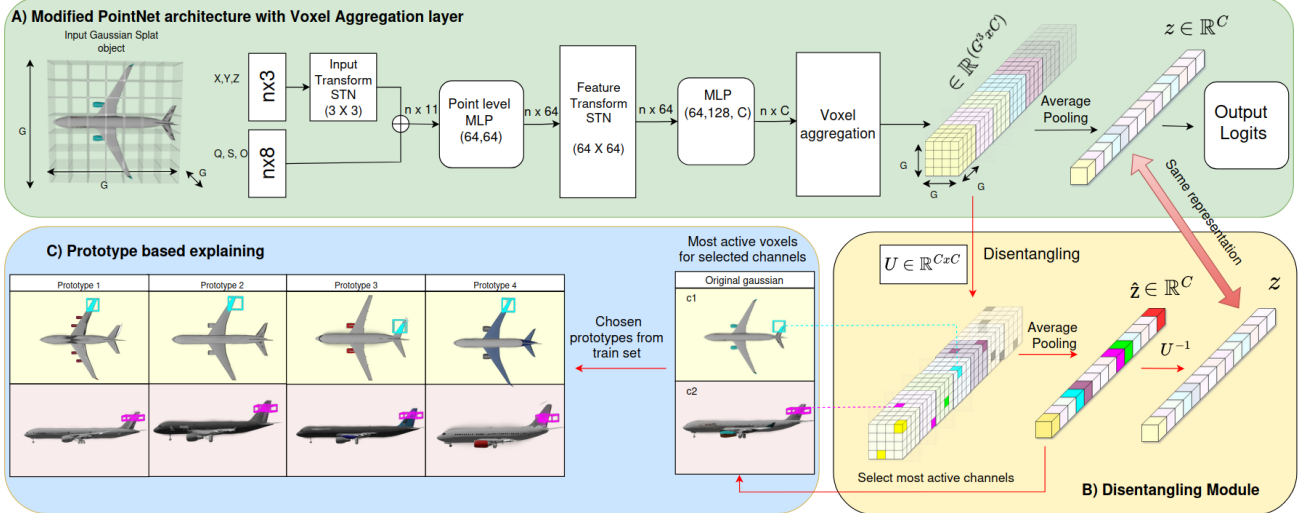


Figure 2. Overview of the XSPLAIN architecture A) The classification backbone is a modified PointNet architecture extended by a voxel aggregation layer, producing structured latent representations at the voxel level from Gaussian Splat inputs. B) An attachable disentangling module learns an invertible linear transformation that separates latent channels for interpretability while preserving the original global representation and classification output. C) Explanations are generated by identifying the most active disentangled channels, visualizing the corresponding influential voxels, and retrieving representative training examples that exhibit similar channel activations.

Global Feature and Classification We obtain the global feature vector by applying average pooling across all voxels:

$$\mathbf{z} = \frac{1}{G^3} \sum_{v=1}^{G^3} \mathbf{h}_v \in \mathbb{R}^C. \quad (4)$$

The final classification is performed by a linear layer:

$$\hat{y} = \arg \max_k (\mathbf{W}_{\text{cls}} \mathbf{z})_k, \quad (5)$$

where $\mathbf{W}_{\text{cls}} \in \mathbb{R}^{K \times C}$ are the classifier weights.

Two-Stage Training Procedure Although the architecture is intrinsically interpretable (ante-hoc), training is performed in two stages to decouple classification from interpretability. Joint optimization of accuracy and prototype purity can reduce discriminative power. Our decoupled strategy preserves backbone feature learning and predictive accuracy while ensuring output-level faithfulness in the second stage.

Stage 1: Backbone Training The entire backbone network is trained f_θ (including both STNs, convolutional layers, voxel aggregation, and the classification head) end-to-end using a combination of classification loss and a density-aware regularization term.

Classification Loss The primary objective is the standard cross-entropy loss:

$$\mathcal{L}_{\text{cls}} = -\frac{1}{|\mathcal{D}|} \sum_{(\mathcal{G}, y) \in \mathcal{D}} \log \frac{\exp((\mathbf{W}_{\text{cls}} \mathbf{z})_y)}{\sum_{k=1}^K \exp((\mathbf{W}_{\text{cls}} \mathbf{z})_k)}, \quad (6)$$

where \mathcal{D} denotes the training dataset.

Density-Aware Regularization The limitation of PointNet-style architectures with max-pooling aggregation is their tendency to focus on isolated outlier points rather than dense, geometrically meaningful regions. In our voxel-based setting, this manifests as high activations in sparsely populated voxels containing only a few Gaussian primitives, which often correspond to reconstruction artifacts or noise rather than salient object parts.

To address this, we introduce a regularization term based on the Kullback-Leibler divergence that encourages the network to align its attention with the spatial density of the input. Let $\mathbf{a} \in \mathbb{R}^{G^3}$ denote the voxel activation magnitudes computed as $a_v = \|\mathbf{h}_v\|_2$, and let $\mathbf{n} \in \mathbb{R}^{G^3}$ denote the point counts per voxel, where $n_v = |\{i : v(i) = v\}|$.

We define two probability distributions over voxels. The activation distribution is obtained by applying a temperature-scaled softmax:

$$p_v = \frac{\exp(\text{ReLU}(a_v)/\tau)}{\sum_{u=1}^{G^3} \exp(\text{ReLU}(a_u)/\tau)}, \quad (7)$$

where $\tau > 0$ is a temperature hyperparameter controlling the sharpness of the distribution. The target density distribution is derived from the point counts:

$$q_v = \frac{n_v^\beta + \epsilon}{\sum_{u=1}^{G^3} (n_u^\beta + \epsilon)}, \quad (8)$$

where $\epsilon = 1 \cdot e^{-6}$ ensures numerical stability and $\beta > 0$ controls sensitivity to density differences

The density-aware regularization is defined as the KL diver-

gence between the target and activation distributions:

$$\mathcal{L}_{\text{density}} = D_{\text{KL}}(p\|q) = \sum_{v=1}^{G^3} p_v \log \frac{p_v}{q_v}. \quad (9)$$

Minimizing this term encourages the model to assign higher activations to voxels with more Gaussian primitives. Intuitively, densely populated voxels are more likely to represent coherent geometric structures (e.g., object surfaces, distinctive parts) rather than isolated outliers or reconstruction noise. This regularization guides the network toward learning features grounded in the actual geometry of the object.

Total Training Objective The complete training objective for Stage 1 combines both terms:

$$\mathcal{L}_{\text{Stage 1}} = \mathcal{L}_{\text{cls}} + \lambda \mathcal{L}_{\text{density}}, \quad (10)$$

where $\lambda \geq 0$ is a hyperparameter balancing classification accuracy and density alignment. This formulation ensures that the learned voxel representations are both discriminative for classification and focused on geometrically meaningful regions, which subsequently benefits the interpretability of the prototype-based explanations in Stage 2.

Stage 2: Parametrized Matrix Training In the second stage, the backbone parameters are frozen and fixed to the solution obtained in the first stage:

$$\theta^* = \arg \min_{\theta} \mathcal{L}_{\text{cls}}(\theta), \quad (11)$$

and no updates of θ are performed during training.

We then introduce a trainable parametrized matrix $\mathbf{U} \in \mathbb{R}^{C \times C}$ inserted between the voxel aggregation module and the global pooling operation. Only the parameters of this matrix are optimized during the second stage on a dynamically updated set of prototype examples (detailed in 3). In this phase, the backbone remains fixed. This design choice ensures that: (1) the classification performance established in Stage 1 is preserved, and (2) the interpretability module does not interfere with learned feature representations.

Parametrized Feature Disentanglement We introduce a transformation matrix $\mathbf{U} \in \mathbb{R}^{C \times C}$ that maps voxel features into a disentangled representation where channels capture semantically distinct information:

$$\tilde{\mathbf{H}} = \mathbf{U} \mathbf{H}_{\text{flat}}, \quad (12)$$

where $\mathbf{H}_{\text{flat}} \in \mathbb{R}^{C \times G^3}$ is the flattened voxel tensor.

To ensure that the transformation preserves the classifier outputs by construction, we restrict it to an orthogonal mapping in the feature space, which preserves inner products and Euclidean distances prior to the fixed classification layer.

Let $\mathbf{P} \in \mathbb{R}^{C \times C}$ be a learnable, unconstrained weight matrix. We derive a skew-symmetric matrix \mathbf{A} and the disentanglement matrix \mathbf{U} as:

$$\mathbf{A} = \mathbf{P} - \mathbf{P}^T. \quad (13)$$

$$\mathbf{U} = \exp(\mathbf{A}). \quad (14)$$

Since \mathbf{A} is skew-symmetric ($\mathbf{A}^T = -\mathbf{A}$), the resulting matrix \mathbf{U} is guaranteed to be orthogonal ($\mathbf{U}^T \mathbf{U} = \mathbf{I}$). Moreover, $\det(\mathbf{U}) = 1$, ensuring the transformation is volume-preserving and strictly invertible. Initializing $\mathbf{P} = \mathbf{0}$, yields $\mathbf{U} = \mathbf{I}$, ensuring the second training stage begins with the exact feature space learned by the backbone.

Classifier Compensation After optimizing \mathbf{P} for interpretability, we compensate the classification head to strictly preserve the original model predictions. Since \mathbf{U} is orthogonal, its inverse is simply its transpose ($\mathbf{U}^{-1} = \mathbf{U}^T$). We compute the adjusted weights as:

$$\mathbf{W}'_{\text{cls}} = \mathbf{W}_{\text{cls}} \mathbf{U}^T. \quad (15)$$

This formulation allows us to rotate the internal feature representation for human interpretation without altering the decision boundary (see Appendix C for proof).

Prototype-Based Interpretability Our interpretability mechanism identifies prototype examples that maximally activate each feature channel.

Prototype Discovery For each channel $c \in \{1, \dots, C\}$, we identify the top- k training samples with the highest activation. For a sample with transformed voxel features $\tilde{\mathbf{H}}$, we compute:

$$a_c = \max_{v:n_v > 0} \tilde{h}_{c,v}, \quad (16)$$

where $\tilde{h}_{c,v}$ is the activation of the c -th channel in voxel v , and n_v is the count of points. We maintain prototype indices $\mathcal{P}_c = \{j_1, \dots, j_k\}$ for the samples with highest a_c .

Purity Metric To train \mathbf{U} toward disentangled representations, we introduce a purity metric measuring how well each channel is isolated in its maximally activated voxel. For a sample associated with channel c :

$$v^* = \arg \max_{v:n_v > 0} \tilde{h}_{c,v}, \quad \text{purity}_c = \frac{\tilde{h}_{c,v^*}}{\|\tilde{\mathbf{h}}_{v^*}\|_2 + \epsilon}. \quad (17)$$

A purity close to 1 indicates that the channel c dominates the representation in its most activated voxel. The training objective maximizes average purity:

$$\mathcal{L}_{\text{purity}} = -\frac{1}{|\mathcal{B}|} \sum_{(i,c) \in \mathcal{B}} \text{purity}_c^{(i)}, \quad (18)$$

where \mathcal{B} is a batch of prototype-channel pairs.

Dynamic Prototype Updates We periodically recompute prototypes during training, using a curriculum that reduces the number per channel:

$$k_t = \left\lfloor k_{\text{init}} - \frac{t}{T}(k_{\text{init}} - k_{\text{final}}) \right\rfloor, \quad (19)$$

for epoch t , allowing the matrix to first capture broad patterns before focusing on representative examples.

Explanation Generation Given a test sample \mathcal{G}^* , we identify the influential channels for the predicted class.

Channel Importance The importance of channel c for the predicted class \hat{y} is:

$$\text{importance}_c = w'_{\hat{y},c} \cdot \text{ReLU}(\tilde{z}_c^*), \quad (20)$$

where $w'_{\hat{y},c}$ is the compensated classifier weight. We select the top- m channels.

Spatial Localization For each important channel c , we localize the explanation by finding the maximally activated voxel index:

$$v_c^* = \arg \max_v \tilde{h}_{c,v}^*. \quad (21)$$

A key advantage of our intrinsic partitioning strategy is the direct reversibility of the spatial attribution. Since the voxel assignment $v(i)$ for each primitive is determined at the input stage and remains invariant to the STN’s alignment transformations, we do not require inverse geometric projections to locate the relevant features. The explanatory subset of primitives \mathcal{E}_c is obtained via a direct lookup:

$$\mathcal{E}_c = \{g_i \in \mathcal{G}^* \mid v(i) = v_c^*\}. \quad (22)$$

We visualize the explanation by rendering only the subset \mathcal{E}_c , allowing for an exact and artifact-free presentation of the regions driving the model’s decision.

4. Experiments

In this section, we validate the effectiveness of XSPLAIN through a comprehensive evaluation involving both qualitative visualizations, quantitative fidelity checks and user study. We utilize a diverse set of data, including a custom version of the synthetic Toys4K dataset (Stojanov et al., 2021), which we converted to 3DGS using TRELLIS (Xiang et al., 2024) (referred to as “Toys”), a subset of ShapeSplat, and the 3D Real Car Toolkit (Du et al., 2024), to assess the method’s ability to capture semantic attributes and distinguish between fine-grained geometric features. In Table 1, we report baseline results for several supervised point cloud architectures, namely PointNet (Charles et al., 2017), PointNet++ (Qi et al., 2017), PointNeXt (Qian et al., 2022) and PointMLP (Ma et al., 2022) after incorporating Gaussian coefficients on these datasets.

Dataset	Model	Accuracy
Toys	PointNet	0.865
Toys	PointNet++	0.934
Toys	PointNeXt	0.898
Toys	PointMLP	0.870
Toys	PointNet + Vox Agg	0.899
MACGS	PointNet	0.873
MACGS	PointNet++	0.871
MACGS	PointNeXt	0.805
MACGS	PointMLP	0.898
MACGS	PointNet + Vox Agg	0.818
Shapesplat	PointNet	0.869
Shapesplat	PointNet++	0.875
Shapesplat	PointNeXt	0.875
Shapesplat	PointMLP	0.803
Shapesplat	PointNet + Vox Agg	0.880

Table 1. Baseline results using supervised point cloud models with additional GS inputs

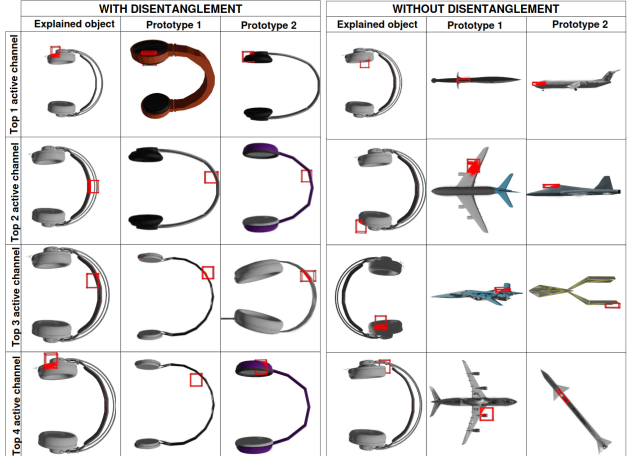


Figure 3. **Left:** Selected prototypes for the most active channels with the disentangling module applied. **Right:** Selected prototypes for the same object without applying the disentangling module.

Prototype Visualization and Interpretability Figure 3 visualizes the behavior of our method on an object from the ShapeSplat dataset, comparing prototype selection with and without the use of the disentangling matrix. For a given target object and a specific feature channel, we identify and highlight the 3DGS voxel with the highest activation for that channel. Each row shows the target object alongside the corresponding fragments from prototype objects that are maximally activated for the same channel. The left panel presents results obtained using the proposed disentangling matrix, whereas the right panel shows the same procedure without applying this matrix. As observed, incorporating the disentangling matrix leads to a markedly stronger semantic and geometric correspondence between the target fragments and the selected prototypes, indicating that the proposed

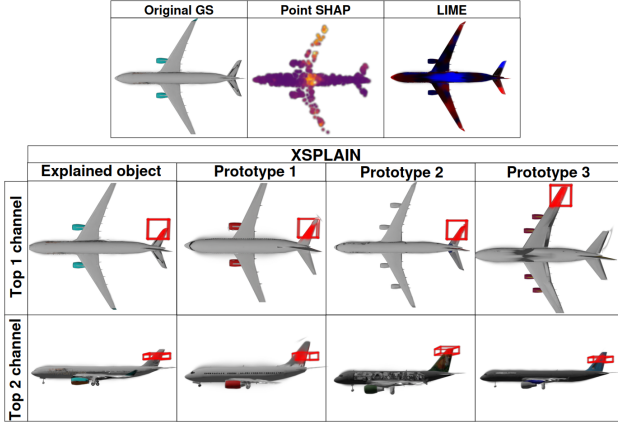


Figure 4. Comparison between PointSHAP, LIME and XSPLAIN explanations

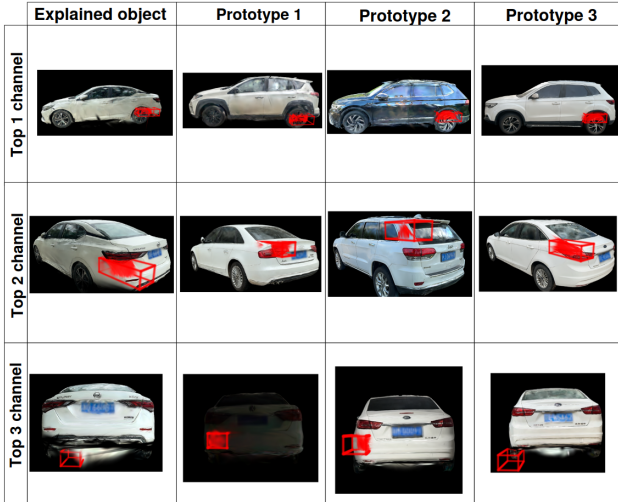


Figure 5. XSPLAIN results on samples from the 3D car dataset.

method more effectively aligns channel-specific geometric attributes across different object instances.

Comparison with Post-Hoc methods We compare XSPLAIN against established post-hoc explanation methods adapted for point-based representations, specifically PointSHAP and LIME. As shown in Figure 4, baseline methods often produce scattered or noisy attributions that fail to respect the underlying object structure. In contrast, XSPLAIN leverages the voxel aggregation mechanism to produce coherent, localized explanations that align better with human intuition regarding object parts. Additional qualitative examples across different object categories and datasets are provided in the appendix E.

Semantic Discrimination We further evaluate the model’s capability to discern subtle geometric differences using real-world datasets. To test the method’s sensitivity to fine-grained features within a superclass, we performed experi-

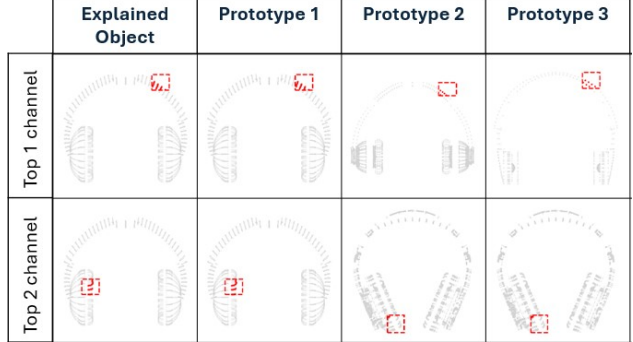


Figure 6. Generalization to ShapeNet Core. The model identifies distinct semantic regions in the point cloud, clearly distinguishing the headband (Row 1) and the ear cups (Row 2).

ments on the 3D Real Car Toolkit (Du et al., 2024). Specifically, we analyzed the model’s ability to distinguish between different vehicle types, such as SUVs and Sedans. Our visualizations in Figure 5 show that the learned features focus on type-specific geometry (e.g., the roofline height or trunk shape), demonstrating that XSPLAIN effectively disentangles intra-class variations crucial for precise classification.

Decoupled vs. Joint Training To validate our 2-stage design choice, we compared XSPLAIN against an end-to-end (one-stage) training strategy. In the 1-stage baseline, the purity loss is minimized concurrently with the classification loss using a mixed-batch approach, where part of each batch consists of prototype candidates. Our experiments reveal that the 1-stage approach leads to a lower classification accuracy than to our decoupled method and prototype selection as shown in Table 2. By freezing the backbone, we ensure that the decision boundaries remain optimal, while the orthogonal transformation \mathbf{U} effectively aligns the latent space for interpretability without sacrificing model performance.

Direct Comparison with Point Clouds A key advantage of XSPLAIN is its versatility. Our method is not limited to 3D Gaussian Splatting but generalizes effectively to standard point cloud data. To validate this, we evaluated our method on the **ShapeNet Core** dataset (Chang et al., 2015) using only geometric features (XYZ coordinates and normals). As shown in Figure 6, the model successfully captures semantic structures (e.g., distinguishing the headband and the ear cups) purely from geometry.

Poll results analysis The poll was performed on $N = 51$ respondents with various background and experience in Machine Learning and XAI domains. LIME (Ribeiro et al., 2016) and SHAP (Lundberg & Lee, 2017) were chosen as competitive methods for two reasons: (i) they provide visual heatmaps that underline regions important for the prediction, in a similar way that XSPLAIN selects most active regions, and (ii) their prevalence in different domains make them a suitable first-choice for any explainability task. The

Method	Hyperparameters		Acc.
	Pool (ρ)	λ_{purity}	
Baseline*	-	-	0.880
XSPLAIN*	-	-	0.880
Joint Opt.	30%	0.5	0.660
Joint Opt.	30%	1.0	0.726
Joint Opt.	50%	0.5	0.625
Joint Opt.	50%	1.0	0.690

Table 2. Impact of training strategy on model performance.

The two-stage approach preserves classification accuracy while improving interpretability, whereas joint optimization (1-stage) fails to balance these objectives. Note: λ_{purity} weights the interpretability loss, and $\text{Pool}(\rho)$ denotes the fraction of training samples used as candidate prototypes. Baseline* represents Raw Backbone and **XSPLAIN*** Decoupled training.

questions varied between two types: (a) the perceived confidence regarding model’s prediction for each method and (b) single-choice preference from proposed explanations. Fig. 7 shows the overall qualitative results with share in each question for categories in (a) and preference for (b). The results showed a significant preference for XSPLAIN with more than 49% of the responses selecting it. More detailed statistical analysis can be found in Appendix B.

Faithfulness and Ablation Study To objectively quantify the faithfulness of our explanations, we performed deletion tests (detailed in Appendix F). By masking the most active voxels associated with the predicted class, we observed a measurable drop in accuracy across all datasets, notably a 6.82% degradation on Toys (Stojanov et al., 2021) and 6.13% on MACGS (Zhang et al., 2025a) when removing top-5 voxels. This confirms that the regions identified by XSPLAIN are indeed critical for the model’s decision making. Finally, our ablation study (Appendix G) highlighted the critical role of density-aware regularization (λ_{den}), which significantly boosts prototype purity by shifting focus from sparse outliers to coherent structures. We further identified a voxel grid resolution of $G = 7$ as the effective balance point between spatial specificity and robustness to sparsity. For the feature dimension, while lower dimensions performed well, we selected $C = 256$ to ensure sufficient latent capacity for disentangling complex semantic attributes.

5. Conclusion

We presented XSPLAIN, an ante-hoc prototype based explainability framework tailored to 3D Gaussian Splat classification that provides spatially grounded and example based rationales without changing the underlying classifier decisions, hence keeping its efficacy. The method combines a voxel aggregated PointNet-style backbone with a trainable orthogonal feature rotation and an exact classifier compensation, which together preserve decision boundaries by

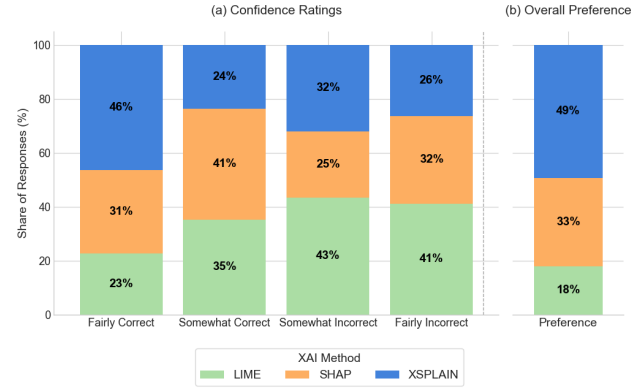


Figure 7. Results of the user study. Question (a) shows the share of each method within specific confidence ratings, highlighting that XSPLAIN dominates the highest confidence category. Question (b) shows the direct user preference share, with XSPLAIN selected half the time.

construction, while reshaping the latent space toward channel wise purity and prototype retrieval. Across evaluated datasets, XSPLAIN maintained the same classification accuracy as the frozen backbone, including 0.880 on ShapeSplat, while improving interpretability as evidenced by large gains in prototype purity and coherent part level localization. In a user study with $N = 51$, users selected XSPLAIN explanations as the best across 3 methods in 48.4% of cases with a statistically significant preference over adapted post-hoc baselines with $p < 0.0001$, indicating higher perceived transparency under realistic inspection conditions. Faithfulness was further supported by deletion tests where removing the top activated voxels reduced accuracy by up to 6.82% on Toys data (a custom 3DGS conversion of Toys4K (Stojanov et al., 2021)), and by 2.36% after removing only the single most influential voxel on MACGS (Zhang et al., 2025a), showing that the highlighted regions carry measurable predictive signal. These results position XSPLAIN as a practical path to interpretable 3DGS recognition that aligns human understandable evidence with model internal mechanisms while avoiding the instability and visual noise typical of saliency-based XAI. Future work may extend the framework to richer and more diverse 3DGS corpora, incorporate appearance and view-dependent attributes when available, and developing stronger quantitative faithfulness and robustness protocols that evaluate explanation stability under controlled perturbations of primitives and under distribution shift. Moreover, a counterfactual (Verma et al., 2024) interpretability investigation would strengthen the claims.

Limitation Note that existing datasets for Gaussian Splatting classification are limited to simple objects (Zhang et al., 2025a), but the fast development of GS-based models increases their importance in a high pace, allowing the method to be tested on a more varied datasets in the future.

6. Acknowledgements

P. Spurek was supported by the project Effective Rendering of 3D Objects Using Gaussian Splatting in an Augmented Reality Environment (FENG.02.02-IP.05-0114/23), carried out under the First Team programme of the Foundation for Polish Science and co-financed by the European Union through the European Funds for Smart Economy 2021–2027 (FENG). The work of P. Borycki was supported by the National Centre of Science (Poland) Grant No. 2025/57/N/ST6/04389. This work has been partially funded by Department of Artificial Intelligence, Wrocław University of Science and Technology. We gratefully acknowledge Poland’s high-performance Infrastructure PLGrid WCSS for providing computer facilities and support within computational grant no. PLG/2025/018654.

References

Arnold, N. I., Angelov, P., and Atkinson, P. M. An improved explainable point cloud classifier (xpcc). *IEEE Transactions on Artificial Intelligence*, 4(1):71–80, 2023. doi: 10.1109/TAI.2022.3150647.

Bach, S., Binder, A., Montavon, G., Klauschen, F., Müller, K.-R., and Samek, W. On pixel-wise explanations for non-linear classifier decisions by layer-wise relevance propagation. *PLoS One*, 10(7):e0130140, 2015.

Bao, Y., Ding, T., Huo, J., Liu, Y., Li, Y., Li, W., Gao, Y., and Luo, J. 3d gaussian splatting: Survey, technologies, challenges, and opportunities. *IEEE Transactions on Circuits and Systems for Video Technology*, 35(7):6832–6852, 2025. doi: 10.1109/TCSVT.2025.3538684.

Borycki, P., Trędowicz, M., Janusz, S., Tabor, J., Spurek, P., Lewicki, A., and Łukasz Struski. Epic: Explanation of pretrained image classification networks via prototype, 2025. URL <https://arxiv.org/abs/2505.12897>.

Buhrmester, V., Münch, D., and Arens, M. Analysis of explainers of black box deep neural networks for computer vision: A survey. *Machine Learning and Knowledge Extraction*, 3(4):966–989, 2021. ISSN 2504-4990. doi: 10.3390/make3040048. URL <https://www.mdpi.com/2504-4990/3/4/48>.

Chang, A. X., Funkhouser, T., Guibas, L., Hanrahan, P., Huang, Q., Li, Z., Savarese, S., Savva, M., Song, S., Su, H., Xiao, J., Yi, L., and Yu, F. ShapeNet: An Information-Rich 3D Model Repository. Technical Report arXiv:1512.03012 [cs.GR], Stanford University — Princeton University — Toyota Technological Institute at Chicago, 2015.

Charles, R. Q., Su, H., Kaichun, M., and Guibas, L. J. Pointnet: Deep learning on point sets for 3d classification and segmentation. In *2017 IEEE Conference on Computer Vision and Pattern Recognition (CVPR)*, pp. 77–85, 2017. doi: 10.1109/CVPR.2017.16.

Chen, C., Li, O., Tao, D., Barnett, A., Rudin, C., and Su, J. K. This looks like that: Deep learning for interpretable image recognition. *Advances in Neural Information Processing Systems*, 32, 2019.

Chen, G. and Wang, W. A survey on 3d gaussian splatting, 2025. URL <https://arxiv.org/abs/2401.03890>.

Crabbé, J., Qian, Z., Imrie, F., and van der Schaar, M. Explaining latent representations with a corpus of examples. *Advances in Neural Information Processing Systems*, 34: 12154–12166, 2021.

Donnelly, J., Barnett, A. J., and Chen, C. Deformable ProtoPNet: An Interpretable Image Classifier Using Deformable Prototypes. In *Proceedings of the IEEE/CVF Conference on Computer Vision and Pattern Recognition (CVPR)*, pp. 10265–10275, 2022.

Du, X., Sun, H., Wang, S., Wu, Z., Sheng, H., Ying, J., Lu, M., Zhu, T., Zhan, K., and Yu, X. 3drealcar: An in-the-wild rgb-d car dataset with 360-degree views. *arXiv preprint arXiv:2406.04875*, 2024.

Feng, T., Quan, R., Wang, X., Wang, W., and Yang, Y. Interpretable3d: An ad-hoc interpretable classifier for 3d point clouds. *Proceedings of the AAAI Conference on Artificial Intelligence*, 38(2):1761–1769, Mar. 2024. doi: 10.1609/aaai.v38i2.27944. URL <https://ojs.aaai.org/index.php/AAAI/article/view/27944>.

Han, C., Lu, Y., Sun, G., Liang, J. C., Cao, Z., Wang, Q., Guan, Q., Dianat, S., Rao, R., Geng, T., Tao, Z., and Liu, D. Prototypical transformer as unified motion learners. In Salakhutdinov, R., Kolter, Z., Heller, K., Weller, A., Oliver, N., Scarlett, J., and Berkenkamp, F. (eds.), *Proceedings of the 41st International Conference on Machine Learning*, volume 235 of *Proceedings of Machine Learning Research*, pp. 17416–17436. PMLR, 21–27 Jul 2024. URL <https://proceedings.mlr.press/v235/han24d.html>.

Jiang, X., Margelou, A., Simidjievski, N., and Jamnik, M. Protogate: prototype-based neural networks with global-to-local feature selection for tabular biomedical data. In *Proceedings of the 41st International Conference on Machine Learning*, ICML’24. JMLR.org, 2024.

Keetha, N., Karhade, J., Jatavallabhula, K. M., Yang, G., Scherer, S., Ramanan, D., and Luiten, J. Splatam: Splat,

track & map 3d gaussians for dense rgb-d slam. In *Proceedings of the IEEE/CVF Conference on Computer Vision and Pattern Recognition*, pp. 21357–21366, 2024.

Kerbl, B., Kopanas, G., Leimkuehler, T., and Drettakis, G. 3d gaussian splatting for real-time radiance field rendering. *ACM Trans. Graph.*, 42(4), July 2023. ISSN 0730-0301. doi: 10.1145/3592433. URL <https://doi.org/10.1145/3592433>.

Koh, P. W., Nguyen, T., Tang, Y. S., Mussmann, S., Pierson, E., Kim, B., and Liang, P. Concept bottleneck models. In *International conference on machine learning*, pp. 5338–5348. PMLR, 2020.

Levi, M. Y. and Gilboa, G. Fast and simple explainability for point cloud networks, 2024. URL <https://arxiv.org/abs/2403.07706>.

Li, F., Zhang, M., Wang, Z., and Yang, M. Infocons: Identifying interpretable critical concepts in point clouds via information theory. *arXiv preprint arXiv:2505.19820*, 2025.

Li, H., Chen, P., et al. Endo-4dgs: Endoscopic gaussian splatting with deformable reconstruction. In *International Conference on Medical Image Computing and Computer-Assisted Intervention*, 2024.

Lundberg, S. M. and Lee, S.-I. A unified approach to interpreting model predictions. *Advances in Neural Information Processing Systems*, 30, 2017.

Ma, Q., Li, Y., Ren, B., Sebe, N., Konukoglu, E., Gevers, T., Van Gool, L., and Paudel, D. P. Shapesplat: A large-scale dataset of gaussian splats and their self-supervised pretraining. *arXiv preprint arXiv:2408.10906*, 2024.

Ma, X., Qin, C., You, H., Ran, H., and Fu, Y. Rethinking network design and local geometry in point cloud: A simple residual mlp framework. *arXiv preprint arXiv:2202.07123*, 2022.

Matrone, F., Paolanti, M., Felicetti, A., Martini, M., and Pierdicca, R. Bubblex: An explainable deep learning framework for point-cloud classification. *IEEE Journal of Selected Topics in Applied Earth Observations and Remote Sensing*, 15:6571–6587, 2022. doi: 10.1109/JSTARS.2022.3195200.

Nauta, L., Sieb, M. H., and van Gemert, J. C. Pipnet: Prototypical part network for interpretable fine-grained recognition. *IEEE Transactions on Pattern Analysis and Machine Intelligence*, 2023.

Nauta, M., van Bree, R., and Seifert, C. Neural prototype trees for interpretable fine-grained image recognition. *2021 IEEE/CVF Conference on Computer Vision and Pattern Recognition (CVPR)*, pp. 14928–14938, 2021.

2020. URL <https://api.semanticscholar.org/CorpusID:227254464>.

Qi, C. R., Yi, L., Su, H., and Guibas, L. J. Pointnet++: Deep hierarchical feature learning on point sets in a metric space. *Advances in neural information processing systems*, 30, 2017.

Qian, G., Li, Y., Peng, H., Mai, J., Hammoud, H., Elhoseiny, M., and Ghanem, B. Pointnext: Revisiting pointnet++ with improved training and scaling strategies. *Advances in neural information processing systems*, 35: 23192–23204, 2022.

Ribeiro, M. T., Singh, S., and Guestrin, C. "why should i trust you?" explaining the predictions of any classifier. In *Proceedings of the 22nd ACM SIGKDD International Conference on Knowledge Discovery and Data Mining*, pp. 1135–1144, 2016.

Rymarczyk, D., Struski, L., Tabor, J., and Zieliński, B. Protopshare: Prototypical parts sharing for similarity discovery in interpretable image classification. In *Proceedings of the 27th ACM SIGKDD Conference on Knowledge Discovery & Data Mining*, KDD '21, pp. 1420–1430, New York, NY, USA, 2021. Association for Computing Machinery. ISBN 9781450383325. doi: 10.1145/3447548.3467245. URL <https://doi.org/10.1145/3447548.3467245>.

Selvaraju, R. R., Cogswell, M., Das, A., Vedantam, R., Parikh, D., and Batra, D. Grad-cam: Visual explanations from deep networks via gradient-based localization. *International Journal of Computer Vision*, 128:336–359, 2020.

Stojanov, S., Thai, A., and Rehg, J. M. Using shape to categorize: Low-shot learning with an explicit shape bias. *2021 IEEE/CVF Conference on Computer Vision and Pattern Recognition (CVPR)*, pp. 1798–1808, 2021. URL <https://api.semanticscholar.org/CorpusID:231639354>.

Struski, Ł., Rymarczyk, D., and Tabor, J. Infodisent: Explainability of image classification models by information disentanglement. *arXiv preprint arXiv:2409.10329*, 2024.

Taghanaki, S. A., Hassani, K., Jayaraman, P. K., Ahmadi, A. H. K., and Custis, T. Pointmask: Towards interpretable and bias-resilient point cloud processing. *CoRR*, abs/2007.04525, 2020. URL <https://arxiv.org/abs/2007.04525>.

Tan, H. and Kotthaus, H. Surrogate model-based explainability methods for point cloud nns. In *2022 IEEE/CVF Winter Conference on Applications of Computer Vision (WACV)*, pp. 2927–2936, 2022. doi: 10.1109/WACV51458.2022.000298.

Ukai, Y., Hirakawa, T., Yamashita, T., and Fujiyoshi, H. This looks like it rather than that: ProtoKNN for similarity-based classifiers. In *The Eleventh International Conference on Learning Representations*, 2023. URL <https://openreview.net/forum?id=1h-HRYxuoRr>.

Verma, S., Boonsanong, V., Hoang, M., Hines, K., Dickerson, J., and Shah, C. Counterfactual explanations and algorithmic recourses for machine learning: A review. *ACM Comput. Surv.*, 56(12), October 2024. ISSN 0360-0300. doi: 10.1145/3677119. URL <https://doi.org/10.1145/3677119>.

Wang, J., Liu, H., Wang, X., and Jing, L. Interpretable image recognition by constructing transparent embedding space. In *2021 IEEE/CVF International Conference on Computer Vision (ICCV)*, pp. 875–884, 2021. doi: 10.1109/ICCV48922.2021.00093.

Xiang, J., Lv, Z., Xu, S., Deng, Y., Wang, R., Zhang, B., Chen, D., Tong, X., and Yang, J. Structured 3d latents for scalable and versatile 3d generation. *arXiv preprint arXiv:2412.01506*, 2024.

Xu, F., Uszkoreit, H., Du, Y., Fan, W., Zhao, D., and Zhu, J. Explainable ai: A brief survey on history, research areas, approaches and challenges. In *Natural Language Processing and Chinese Computing*, pp. 563–574. Springer, 2019.

Zhang, B., Huang, S., Shen, W., and Wei, Z. Explaining the pointnet: What has been learned inside the pointnet? In *Proceedings of the IEEE/CVF Conference on Computer Vision and Pattern Recognition (CVPR) Workshops*, June 2019.

Zhang, R., Zhu, H., Zhao, J., Zhang, Q., Cao, X., and Ma, Z. Mitigating ambiguities in 3d classification with gaussian splatting. In *Proceedings of the Computer Vision and Pattern Recognition Conference*, pp. 27275–27284, 2025a.

Zhang, Y., Xie, B., Zhu, H., Wang, Q., Guo, H., Jin, X., and Zeng, W. Interpretable single-view 3d gaussian splatting using unsupervised hierarchical disentangled representation learning. *arXiv preprint arXiv:2504.04190*, 2025b.

Zhou, X., Lin, Z., Shan, X., Wang, Y., Sun, D., and Yang, M.-H. Drivinggaussian: Composite gaussian splatting for surround-view autonomous driving scenes. In *Proceedings of the IEEE/CVF Conference on Computer Vision and Pattern Recognition*, pp. 21634–21643, 2024.

A. Structure of the Poll

The user study was conducted using a Google Form interface to ensure accessibility and standardization. Participants were presented with a series of questions, each featuring two distinct types of visual stimuli displayed as animated GIFs. For every query, the interface displayed three anonymized methods: Method A, Method B, and Method C.

Unbeknownst to the participants, the labels were fixed: Method C always represented our proposed XSPLAIN framework (incorporating the original query and prototypes), while Methods A and B represented baseline approaches.

Below, you see three different explanations for the same model prediction, shown * separately.

Based on the explanations shown, which one helps you better understand *why* the model made its prediction?

- Method A
- Method B
- Method C

Original, Method A, Method B

Original	Method_A	Method_B
----------	----------	----------



Method C



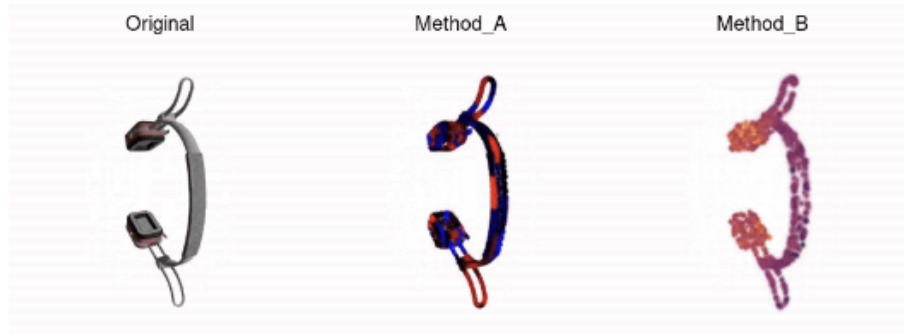
Figure 8. An exemplary view of the survey interface used to evaluate the quality of explanations across different methods.

(Images below) A rendered 3D object has been classified by the model. Along with the rendering, the model provides an explanation intended to justify its prediction. Based on explanation method, how confident are you in the correctness of the model's classification? *

	Fairly confident that the model is correct	Somewhat confident that the model is correct	Somewhat confident that the model is incorrect	Fairly confident that the model is incorrect
Method A	<input type="radio"/>	<input type="radio"/>	<input type="radio"/>	<input type="radio"/>
Method B	<input type="radio"/>	<input type="radio"/>	<input type="radio"/>	<input type="radio"/>
Method C	<input type="radio"/>	<input type="radio"/>	<input type="radio"/>	<input type="radio"/>



Original, Method A, Method B



Method C



Figure 9. An exemplary view of the survey interface where participants rated how strongly the provided explanation convinced them of the classification's correctness.

B. Extended analysis of the responses

B.1. Data structure and inferential targets

We collected full responses from $N = 51$ respondents. The study group consisted of 6 women and 45 men. Regarding Machine Learning expertise, the majority were intermediate ($N_{i,ML} = 26$) or advanced ($N_{a,ML} = 14$) practitioners, with the remainder being beginners ($N_{b,ML} = 9$) or having no experience ($N_{0,ML} = 2$). Experience with 3D modelling was more limited, with most participants identifying as beginners ($N_{b,3D} = 22$) or having no experience ($N_{0,3D} = 21$), and only 8 intermediate users. Familiarity with Explainable AI (XAI) was mixed: 23 participants had no prior experience, while the rest were intermediate ($N_{i,XAI} = 16$), beginners ($N_{b,XAI} = 11$), or advanced ($N_{a,XAI} = 1$) users. Each respondent evaluated 3 separate items. In each item, the respondent saw 3 explanation methods, denoted Method A, Method B, and Method C. The methods behind the notation were hidden from the respondents and denoted Lime (Ribeiro et al., 2016) by A, PointSHAP (Lundberg & Lee, 2017) by B, and XSPLAIN by C. Two information were collected per item.

1. **Best method selection:** a single categorical choice among $\{A, B, C\}$.
2. **Confidence rating:** a four level confidence rating, mapped to integers ("Fairly confident correct" to 4, "Somewhat confident correct" to 3, "Somewhat confident incorrect" to 2, "Fairly confident incorrect" maps to 1) that the selected explanation supports a correct understanding.

Statistical analysis follows a deliberate sequence that mirrors these measurement properties. First, for the categorical selection outcome, the primary question is whether the population choice probabilities differ from the uniform allocation across three categories. This motivates a goodness of fit test within each item. After establishing whether non-uniformity exists in an item, the analysis proceeds to pairwise contrasts to identify which methods differ, with Holm correction to control familywise error within the set of three pairwise comparisons. Second, for confidence, the data are repeated measures because each respondent rates all 3 methods within the same item. The primary question is whether confidence differs systematically across methods within an item. This motivates a repeated measures omnibus test, specifically the Friedman test, followed by paired Wilcoxon signed rank comparisons with Holm correction only when the omnibus result is statistically significant.

Throughout, the nominal significance level is $\alpha = 0.05$. Holm correction is applied separately within each family of pairwise tests, meaning within one item for the selection comparisons and within one confidence block for the confidence comparisons.

Note that the 2 outcomes require different inferential tools as they encode different forms of replication. Within a fixed item, the $N = 51$ observations are naturally treated as independent across respondents, because each respondent contributes exactly one choice for the best method. The dependence problem appears only when we stack across items, because then each respondent contributes 3 choices and those can be correlated within the same person. For the confidence, the dependence exists already within each item, as each respondent rates all 3 methods in the same context. The 3 ratings from one respondent may not be independent, hence we include repeated measures inference, which explicitly accounts for within-respondent coupling by comparing methods of each respondent and then aggregating evidence across respondents. To account for this we use χ^2 goodness of fit for item level selections, and Friedman and Wilcoxon procedures for confidence ratings. Each method matches the sampling unit and the dependence structure of the corresponding outcome.

B.2. Best method selection

For each item, let (X_A, X_B, X_C) denote the counts of best method selection for each of the items, across the $N = 51$ respondents, naturally, $X_A + X_B + X_C = N$. The null hypothesis for each item is uniform choice probabilities

$$H_0 : p_A = p_B = p_C = \frac{1}{3}.$$

Under H_0 , the expected count in each category is $E_j = N/3$. The omnibus test is Pearson's χ^2 goodness of fit statistic

$$\chi^2 = \sum_{j \in \{A, B, C\}} \frac{(X_j - E_j)^2}{E_j},$$

which is asymptotically χ^2 distributed with $k - 1 = 2$ degrees of freedom.

For each of the items, we obtained rejections of the hypothesis of uniformity at $\alpha = 0.05$ for the two first items. The hypothesis could not be rejected for the third item.

- **Item 1:** $(X_A, X_B, X_C) = (9, 16, 26)$, $\chi^2 = 8.588$, $p = 0.01365$.
- **Item 2:** $(X_A, X_B, X_C) = (8, 18, 25)$, $\chi^2 = 8.588$, $p = 0.01365$.
- **Item 3:** $(X_A, X_B, X_C) = (11, 17, 23)$, $\chi^2 = 4.235$, $p = 0.1203$.

Following a significant omnibus test, the script we performed pairwise comparisons and applied Holm correction for controlling false positives among the three pairwise contrasts for a given item. For the first item, Holm-corrected post-hoc tests found a difference between selection of methods A and C ($p = 0.001176$), while comparisons involving B were not significant after correction ($p = 0.107109$ for A vs B, and $p = 0.088467$ B vs C). With the second item, Holm-corrected post-hoc tests found differences in selection of A versus C ($p = 0.000962$) and A versus B ($p = 0.046174$). The comparison B versus C was not significant after correction with $p = 0.160443$. Due to the results, we desided to perform the analysis of the joint selection in the poll.

Stacked selection analysis across items If the three items are stacked, each respondent contributes three selections, yielding $n = 3N = 153$ total selections with counts

$$(X_A, X_B, X_C) = (28, 51, 74).$$

The χ^2 goodness of fit test against uniformity yields $\chi^2 = 20.745$ and $p = 3.128 \times 10^{-5}$, which is strong evidence against uniform choice probabilities. The stacked test treats the $n = 153$ selections as independent and identically distributed. This is not strictly correct because each respondent contributes 3 observation. The strong χ^2 signal and consistent directionality across items suggests robustness, but the p-value from the stacked test is approximated. The present conclusions values should be taken as strong evidence of preferential selection for Method C, with p-values understood as approximate under within respondent dependence. What is important, Holm correction keeps the order of magnitude for each of the compaired pairs in the stacked test, i.e., $p = 7.285604 \times 10^{-8}$ after correction and $p = 2.428535 \times 10^{-8}$ pre-correction for A vs C, $p = 5.321581 \times 10^{-3}$ after correction and $p = 2.660791 \times 10^{-3}$ pre-correction for A vs B, as well as $p = 7.476980 \times 10^{-3}$ both before and after correction for B vs C, indicating that all 3 pairs differ jointly across all the items. We decided to investigate the size of this effect with Cramér's $V = \sqrt{\frac{\chi^2}{n(k-1)}} = \sqrt{\frac{20.745}{153 \cdot 2}} = 0.2604$, which corresponds to a small to moderate association magnitude for a 3-category outcome.

Confidence intervals for selection proportions Let $\hat{p}_m = X_m/n$ for method $m \in \{A, B, C\}$ under the stacked view. The reported 95% Wilson score intervals are:

$$\begin{aligned} \hat{p}_A &= \frac{28}{153} = 0.183, & \text{CI}_{0.95} &= [0.130, 0.252], \\ \hat{p}_B &= \frac{51}{153} = 0.333, & \text{CI}_{0.95} &= [0.264, 0.411], \\ \hat{p}_C &= \frac{74}{153} = 0.484, & \text{CI}_{0.95} &= [0.406, 0.562]. \end{aligned}$$

The intervals quantify uncertainty in the marginal choice rates under the stacked view *under the working independence model for the stacked data*. Method C has the highest estimated selection probability and its interval lies well above $\frac{1}{3}$, while Method A lies below $\frac{1}{3}$. Note that due to within-respondent dependence mentioned earlier, they can be slightly too narrow. Note that given the number of samples the working assumption of independence is more suitable than bootstrapping. We further analyzed the selections of the best method in the demographic groups defined by self-reported Machine Learning experience and by self-reported XAI experience. Groups with $n < 8$ were excluded from inference.

By Machine Learning experience.

- Beginner, $N = 9$, stacked counts $(6, 6, 15)$ across $n = 27$ selections. Performing the omnibus test resulted in $\chi^2 = 6.000$, $p = 0.04979$. Holm-corrected post-hoc tests indicate Method C is selected more often than A ($p = 0.035983$) and more often than B ($p = 0.035983$), with Wilson interval

$$p_C = 15/27 = 0.556, \text{ CI}_{0.95} = [0.373, 0.724].$$

Cramér's $V = \sqrt{6/(27 \cdot 2)} = \frac{1}{3}$, showing moderate magnitude.

- Intermediate, $N = 26$, stacked counts (16, 32, 30) across $n = 78$ selections. Performing the omnibus test resulted in $\chi^2 = 5.846$, $p = 0.05377$, not significant at $\alpha = 0.05$, hence no post-hoc claims were performed.
- Advanced, $N = 14$, stacked counts (6, 10, 26) across $n = 42$ selections. Performing the omnibus test resulted in $\chi^2 = 16.000$, $p = 0.0003355$. Holm-corrected post-hoc tests show Method C exceeds both A ($p = 0.000021$) and B ($p = 0.000838$), while no significance was found in difference between A and B (pre- and post-Holm correction $p = 0.266380$). Wilson interval for Method C is

$$p_C = 26/42 = 0.619, \text{ CI}_{0.95} = [0.468, 0.750].$$

Cramér's $V = \sqrt{16/(42 \cdot 2)} \approx 0.4364$, indicating a moderate association magnitude.

Overall, the preference for Method C is clearest in the Advanced and Beginner groups, while the Intermediate group shows a similar direction but does not reach the $\alpha = 0.05$ threshold in the stacked test. Note that we can claim that explaining the model's difference might be of the most importance for those that are the most and the least experienced. **By XAI experience.**

- None, $N = 23$, stacked counts (14, 19, 36) across $n = 69$ selections. Omnibus $\chi^2 = 11.565$, $p = 0.003081$. Holm-corrected post-hoc tests show Method C exceeds A ($p = 0.000293$) and exceeds B ($p = 0.006238$), with A versus B showing $p = 0.318360$. Wilson interval for Method C is

$$p_C = 36/69 = 0.522, \text{ CI}_{0.95} = [0.406, 0.635].$$

- Beginner, $N = 11$, stacked counts (7, 13, 13) across $n = 33$ selections. Omnibus $\chi^2 = 2.182$, $p = 0.3359$, hence there was no evidence against uniformity.
- Intermediate, $N = 16$, stacked counts (7, 18, 23) across $n = 48$ selections. Omnibus $\chi^2 = 8.375$, $p = 0.01518$. Holm-corrected post-hoc tests show Method A is selected less often than B ($p = 0.021045$) and less often than C ($p = 0.001280$), while B versus C is not significant ($p = 0.302236$). Wilson intervals include

$$p_A = 7/48 = 0.146, \text{ CI}_{0.95} = [0.072, 0.272].$$

B.3. Confidence ratings

Confidence ratings were assumed as numbers in Likert scale 1-4, hence are ordinal and not normally distributed in most blocks according to Shapiro results. Therefore the primary omnibus test is Friedman repeated measures, which tests equality of the marginal distributions across methods within each block.

Effect size is Kendall's $W = \chi^2/(n(k - 1))$ with $k = 3$, with values near 0 indicating weak consistency of method ranking across respondents, values closer to 1 indicate strong agreement.

- Confidence on 1st item, $n = 51$, Friedman $\chi^2 = 2.872$, $p = 0.2379$, $W = 0.028$. This suggests no significant evidence of differences in the subject reported confidence across methods.
- Confidence on 2nd item, $n = 51$, Friedman $\chi^2 = 12.896$, $p = 0.001584$, $W = 0.126$. Post-hoc Wilcoxon tests with Holm correction indicate a significant difference between Method A and Method C, with median difference A minus C equal to -1 . This indicates higher confidence under Method C than under Method A by about one Likert level in median. Other pairwise comparisons were not significant after correction.
- Confidence on 3rd item, $n = 51$, Friedman $\chi^2 = 2.747$, $p = 0.2532$, $W = 0.027$. Showed no significant evidence of differences in the subject reported confidence across methods.

Additionally, a per respondent mean confidence across blocks was computed for each method and tested with Friedman. With $n = 51$, Friedman $\chi^2 = 3.841$, $p = 0.1465$, $W = 0.038$, indicating no detectable overall shift in confidence when averaging across the three items.

For paired confidence ratings, effect sizes were quantified using the Hodges-Lehmann estimator of the paired shift. For each respondent and item, paired differences were computed as

$$d_i = \text{Confidence}_{i,A} - \text{Confidence}_{i,C}, \quad i = 1, \dots, 51.$$

The HL estimator is defined as the median of the paired differences $\hat{\Delta}_{HL} = \text{median}(d_1, \dots, d_{51})$, and estimates the shift in confidence between Method A and Method C on the Likert scale. Uncertainty was quantified using nonparametric bootstrap confidence intervals obtained by resampling respondents with replacement and recomputing the HL estimator. For the second item, the HL estimator was $\hat{\Delta}_{HL} = -1$ with a 95% confidence interval of $[-1, 0]$. This indicates that the typical respondent reported approximately one Likert level higher confidence under Method C than under Method A. The confidence interval excludes positive values and is consistent with the significant Friedman omnibus test and the Holm-corrected Wilcoxon signed-rank test for this item. While for the other two items we calculated $\hat{\Delta}_{HL} = 0$ indicating no significant differences in the confidence, as suggested by the non-significant Friedman test result. The 95% confidence interval was equal to $[-1, 1]$ in the first item, and $[-1, 0]$ in the third.

Subgroup confidence results. Subgroup analyses mostly mirror the overall pattern. For Machine Learning and Deep Learning Intermediate group, 2nd item shows Friedman significance with $p = 0.002271$ and $W = 0.234$, and the post-hoc A versus C comparison remains significant after Holm correction with median difference -1 . Other blocks and the aggregated analysis are not significant. Whereas for Machine Learning Advanced and Beginner groups, no confidence block shows a Holm-corrected significant pairwise difference.

For groups divided by XAI familiarity, None, Intermediate, and Beginner groups showed no Holm-corrected pairwise differences in confidence scale, although XAI Intermediate has an omnibus Friedman $p = 0.02538$ in the second item that does not translate to Holm-corrected pairwise significance.

C. Classifier Compensation Proof

We show that the classifier compensation preserves the original model predictions exactly. Let $\tilde{\mathbf{z}} = \mathbf{U}\mathbf{z}$ denote the transformed global feature, where \mathbf{U} is the orthogonal disentanglement matrix and \mathbf{z} is the original global feature vector.

After compensation, the classifier weights become $\mathbf{W}'_{\text{cls}} = \mathbf{W}_{\text{cls}}\mathbf{U}^T$. The prediction on the transformed features is:

$$\mathbf{W}'_{\text{cls}}\tilde{\mathbf{z}} = (\mathbf{W}_{\text{cls}}\mathbf{U}^T)(\mathbf{U}\mathbf{z}) \quad (23)$$

$$= \mathbf{W}_{\text{cls}}(\mathbf{U}^T\mathbf{U})\mathbf{z} \quad (24)$$

$$= \mathbf{W}_{\text{cls}}\mathbf{I}\mathbf{z} \quad (25)$$

$$= \mathbf{W}_{\text{cls}}\mathbf{z}, \quad (26)$$

where the third equality follows from the orthogonality of \mathbf{U} ($\mathbf{U}^T\mathbf{U} = \mathbf{I}$).

Thus, the logits and consequently the predicted class remain identical before and after applying the disentanglement transformation, ensuring that the interpretability module does not affect the model's decisions.

D. Additional Details on Point Cloud Generalization

Expanding on the generalization capabilities discussed in the main text, here we provide further quantitative and qualitative details regarding the experiments on standard point clouds. While our primary evaluation focuses on the rich 3D Gaussian Splatting representation, verifying performance on the **ShapeNet Core** dataset (Chang et al., 2015) demonstrates that XSPLAIN is not limited to 3D Gaussian Splatting objects.

Experimental Setup. To isolate geometric understanding from rendering attributes, we trained the model on raw point cloud data consisting of N points. The input features were limited to spatial coordinates and surface normals ($N \times 6$ features: x, y, z, n_x, n_y, n_z). **We utilized the same default hyperparameter configuration as in our main experiments: density regularization $\lambda = 3.5$, voxel grid size $G = 7$, and latent feature dimension $C = 256$.**

Quantitative Results. The model demonstrated high stability and effectiveness in this setting. The PointNet backbone achieved a **classification accuracy of 94.4%**. The **purity metric** increased from **13.0%** to **22.5%** during the training of the orthogonal matrix.

Qualitative Results. Visualizations of the learned prototypes confirm that the method successfully captures semantic parts based purely on geometry. As shown in Figures 10, 11, 12 and 13, the active channels clearly distinguish between structural components, such as separating airplane wings or the ear cups of headphones, without relying on color or opacity cues.

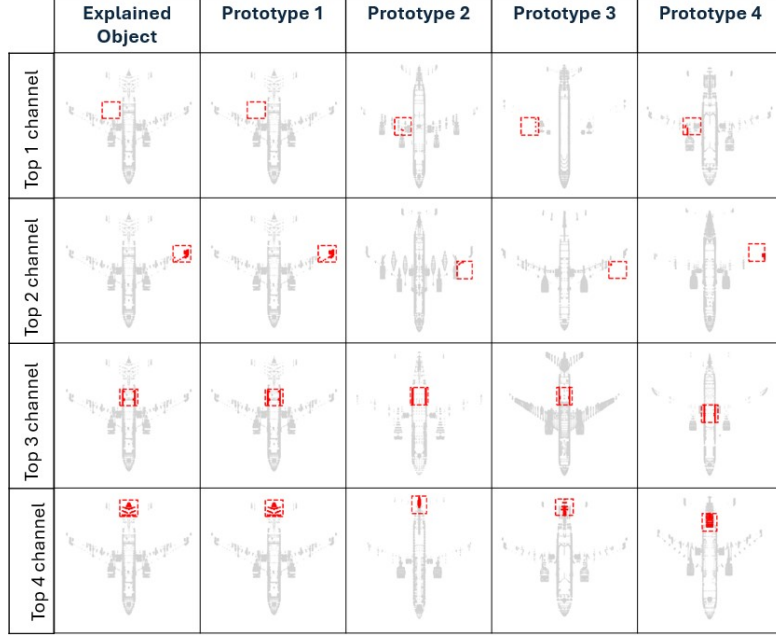


Figure 10. **XSPLAIN explanation** illustrating four prototypes corresponding to the four most active channels for an object from the Airplane class in the ShapeNet Core dataset.

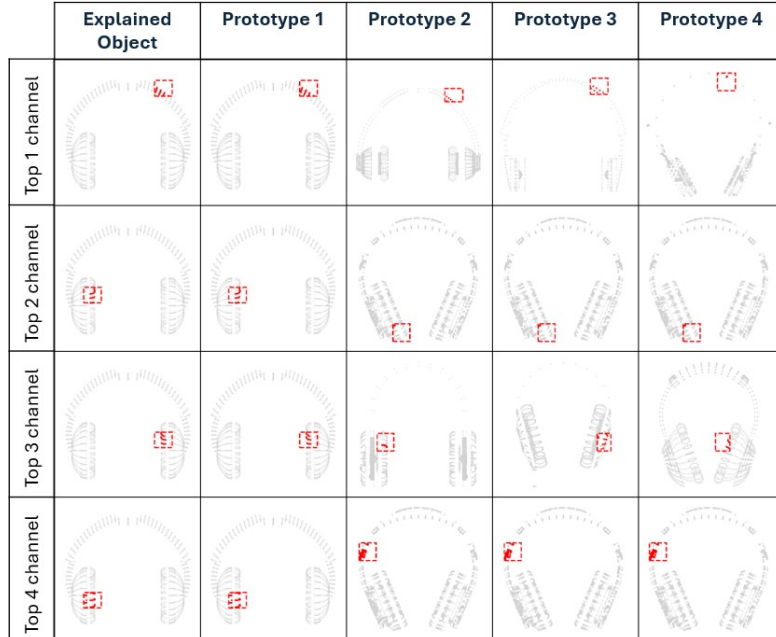


Figure 11. **XSPLAIN explanation** illustrating four prototypes corresponding to the four most active channels for an object from the Earphones class in the ShapeNet Core dataset.

Explained Object	Prototype 1	Prototype 2	Prototype 3	Prototype 4
Top 1 channel				
Top 2 channel				
Top 3 channel				
Top 4 channel				

Figure 12. **XSPLAIN explanation** illustrating four prototypes corresponding to the four most active channels for an object from the *Guitar* class in the ShapeNet Core dataset.

Explained Object	Prototype 1	Prototype 2	Prototype 3	Prototype 4
Top 1 channel				
Top 2 channel				
Top 3 channel				
Top 4 channel				

Figure 13. **XSPLAIN explanation** illustrating four prototypes corresponding to the four most active channels for an object from the *Skateboard* class in the ShapeNet Core dataset.

E. Additional Explaining Examples

In this section, we present extended qualitative comparisons between XSPLAIN and post-hoc baseline methods (PointSHAP and LIME). We visualize results across diverse object categories selected from three distinct datasets used in our main evaluation: **ShapeSplat** (Ma et al., 2024), the **Toys** dataset (a custom 3DGS conversion of Toys4K (Stojanov et al., 2021)), and the **3D Real Car Toolkit** (Du et al., 2024).

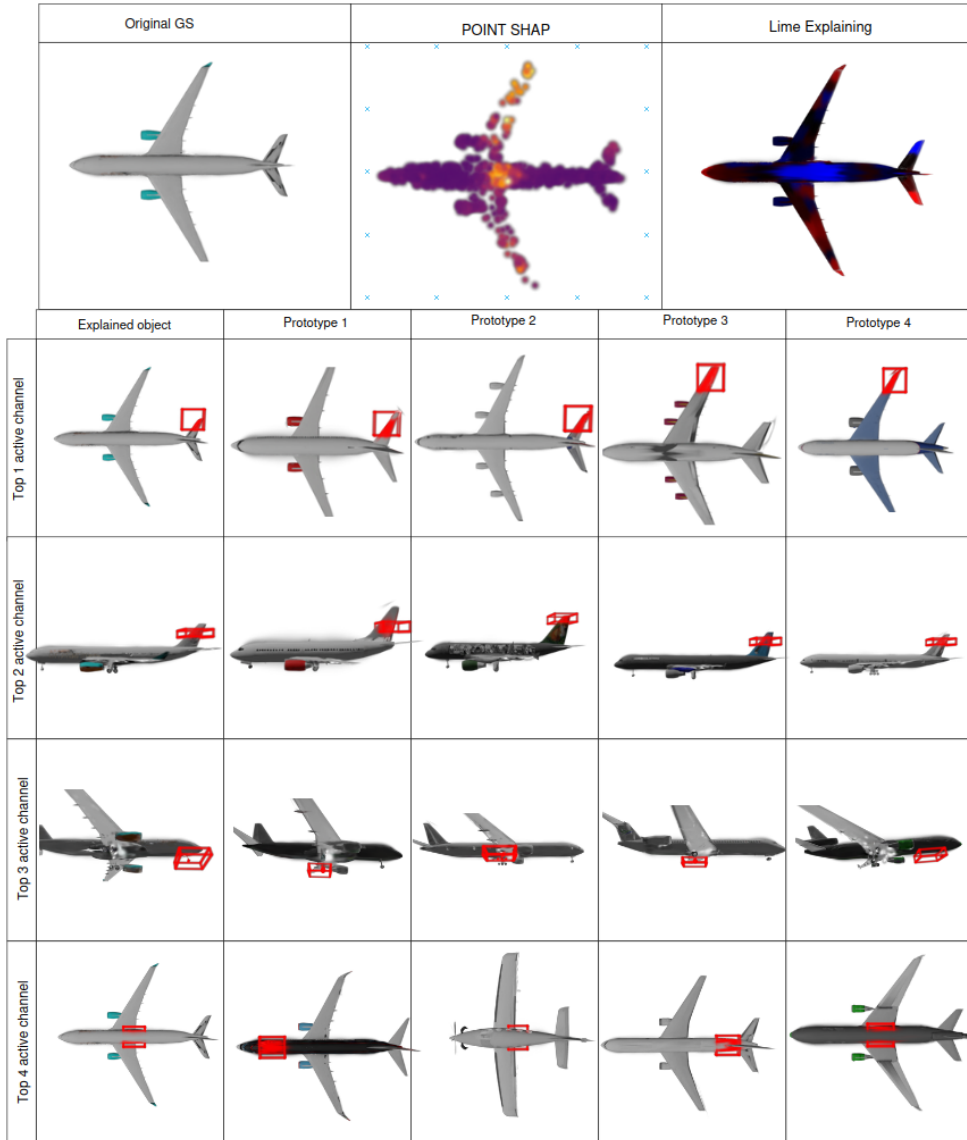


Figure 14. XSPLAIN explanation using four prototypes corresponding to the four most active channels, compared with PointSHAP and LIME for an object from airplane class from the ShapeSplat dataset.

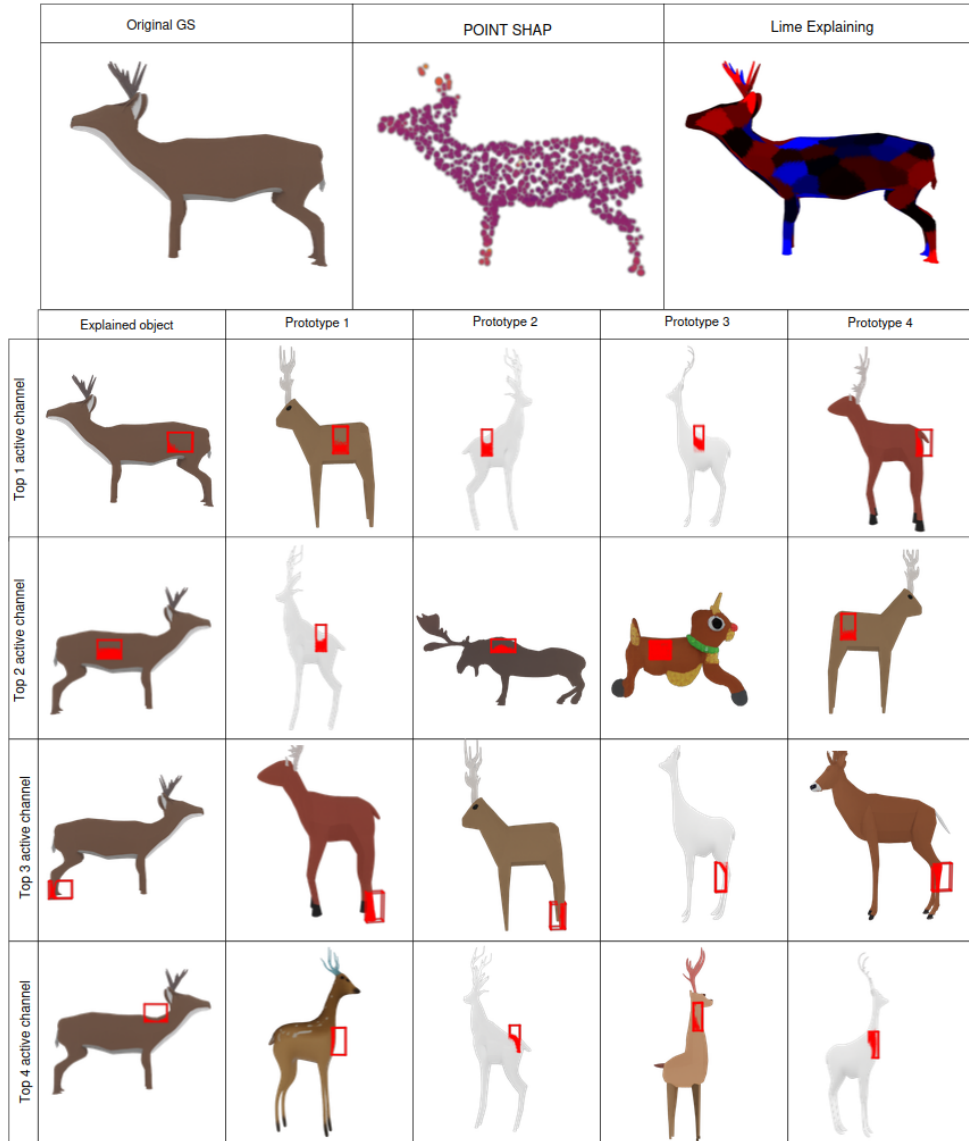


Figure 15. XSPLAIN explanation using four prototypes corresponding to the four most active channels, compared with PointSHAP and LIME for an object from deer moose class from the Toys dataset.

Original GS	POINT SHAP	Lime Explaining			
					
Explained object	Prototype 1	Prototype 2	Prototype 3	Prototype 4	
Top 1 active channel					
Top 2 active channel					
Top 3 active channel					
Top 4 active channel					

Figure 16. XSPLAIN explanation using four prototypes corresponding to the four most active channels, compared with PointSHAP and LIME for an object from the sedan class from the 3d_cars dataset.



Figure 17. XSPLAIN explanation using four prototypes corresponding to the four most active channels, compared with PointSHAP and LIME for an object from earphone class from the ShapeSplat dataset.

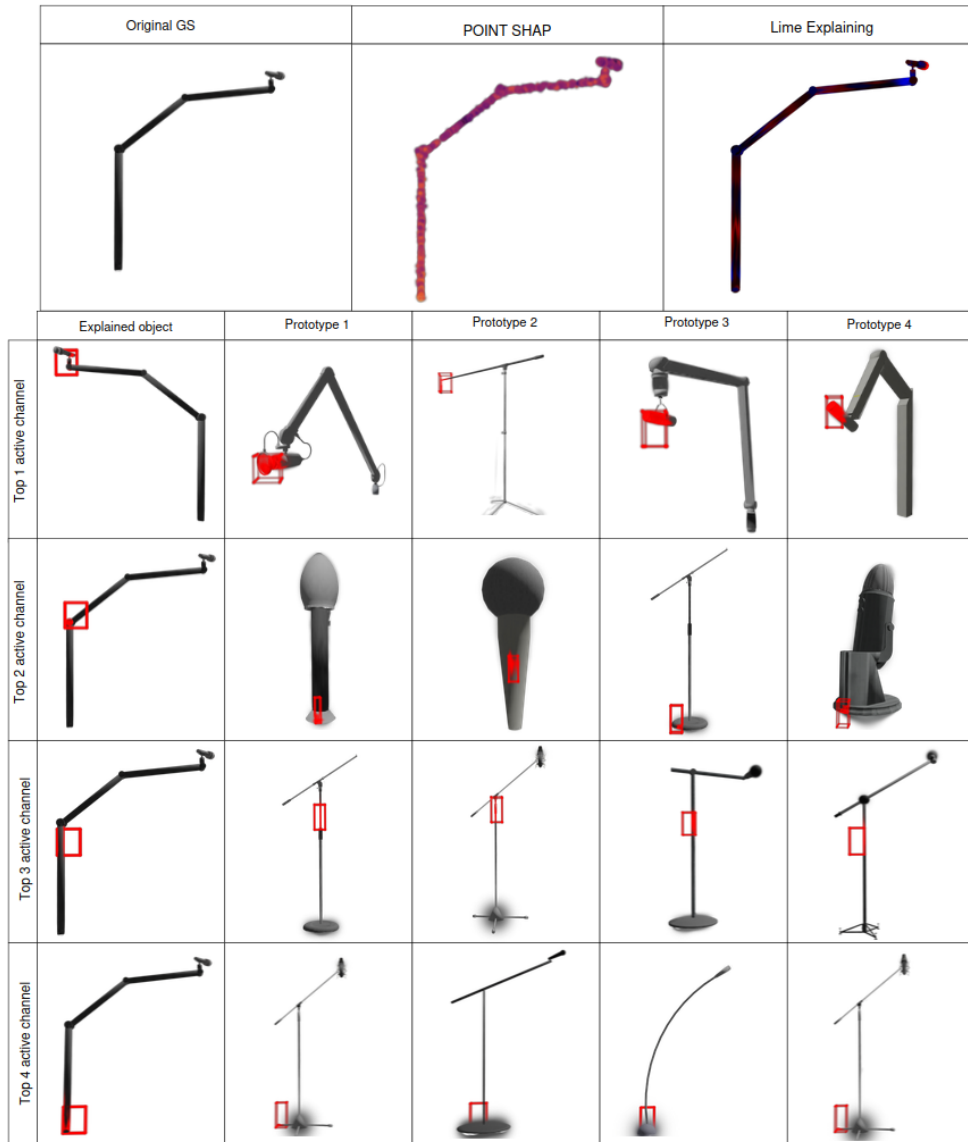


Figure 18. XSPLAIN explanation using four prototypes corresponding to the four most active channels, compared with PointSHAP and LIME for an object from microphone class from the ShapeSplat dataset.

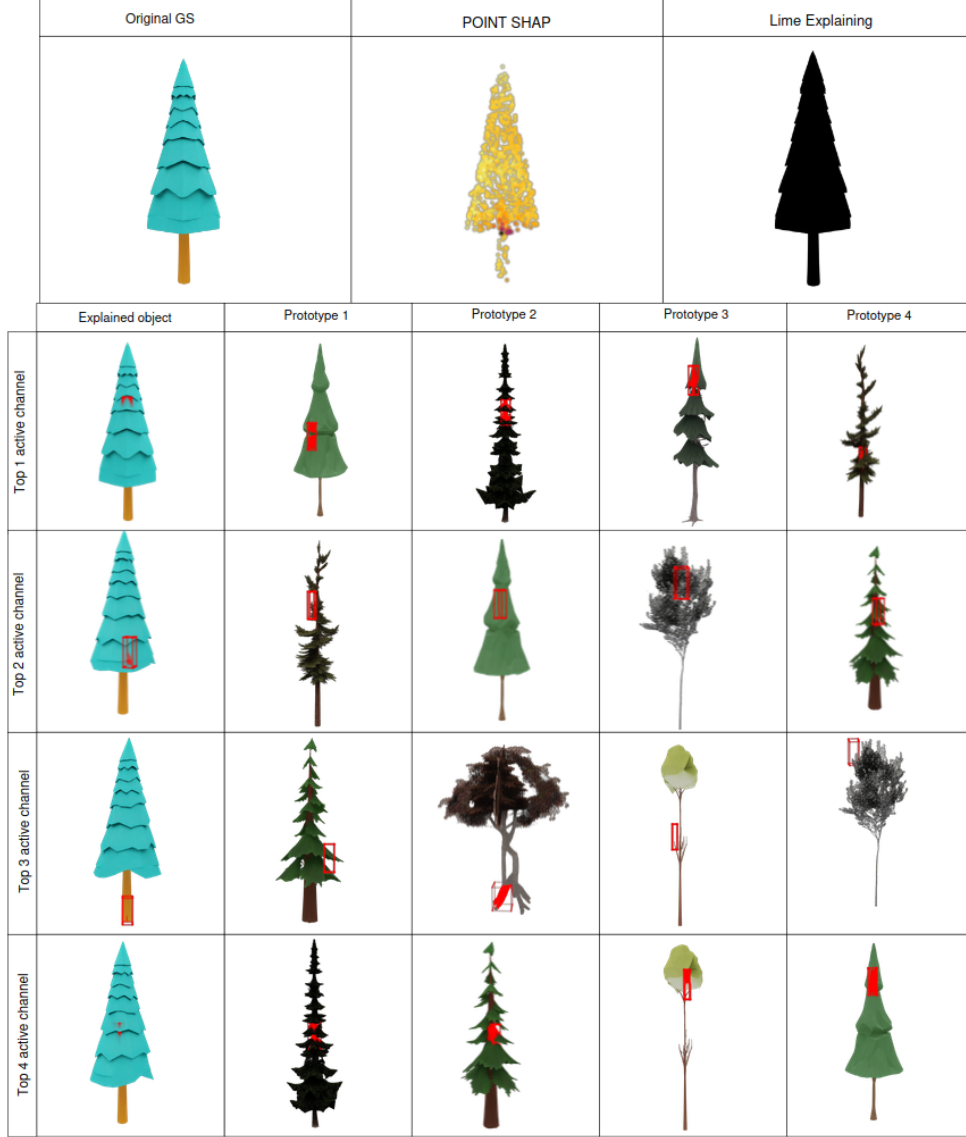


Figure 19. XSPLAIN explanation using four prototypes corresponding to the four most active channels, compared with PointSHAP and LIME for an object from tree class from the Toys dataset.

F. Deletion Test

To evaluate the importance of voxels selected for channel prototypes, we evaluated the accuracy of samples with the top k voxels, corresponding to the top k activated channels, completely removed from the input. Table 3 shows that indeed removing important voxels influences the final accuracy.

Dataset	Top k	Perturbation degradation
MACGS	1	2.36%
MACGS	2	5.66%
MACGS	3	5.66%
MACGS	4	5.19%
MACGS	5	6.13%
Shapesplat	1	1.46%
Shapesplat	2	2.19%
Shapesplat	3	0.73%
Shapesplat	4	1.46%
Shapesplat	5	1.46%
Toys	1	4.55%
Toys	2	4.55%
Toys	3	5.68%
Toys	4	4.55%
Toys	5	6.82%

Table 3. Degradation in accuracy (as relative percentage change) after perturbing top k most active voxels in each sample, for each dataset.

G. Hyperparameters

We performed a comprehensive ablation study on the **ShapeSplat** dataset to analyze the impact of key hyperparameters on both classification performance and explanation quality. The results highlight the trade-off between pure accuracy and the interpretability metrics (Purity Gain and Voxel Density).

Analysis

- Regularization (λ_{den}): Without density regularization ($\lambda = 0$), the model achieves higher accuracy but focuses on sparse outliers (Density=32), leading to poor interpretability. Increasing λ forces the model to focus on dense, geometric regions, significantly boosting Purity Gain.
- Grid Size (G): A resolution of $G = 7$ offers the best balance. Coarser grids ($G = 3$) lack spatial specificity, while finer grids ($G = 15$) result in sparse voxels susceptible to noise.
- Feature Dimension (C): While $C = 64$ yields maximum accuracy, we utilize $C = 256$ as the default to ensure sufficient capacity to disentangle complex semantic attributes during the interpretation stage.

Param.	Val.	Acc.	Pur. Gain	Dens.
Reg. Strength (λ_{den})	0.0	86.3	+37.1%	32
	1.0	84.5	+86.3%	78
	2.0	78.5	+67.3%	75
	3.5 [†]	82.1	+61.1%	78
	5.0	83.9	+66.0%	79
Grid Res. (G)	3	83.3	+55.3%	468
	5	77.3	+62.1%	158
	7 [†]	82.1	+61.1%	78
	10	81.5	+54.9%	36
	15	78.5	+51.1%	23
Feat. Dim. (C)	16	85.7	+36.0%	74
	64	88.0	+64.1%	74
	256 [†]	82.1	+61.1%	78
	1024	66.6	+46.3%	72

Table 4. **Ablation Study.** **Acc.:** Classification Accuracy (%), **Pur. Gain:** Relative improvement in prototype purity after Stage 2 optimization, **Dens.:** Mean point count in activated voxels. ([†]) indicates the default configuration.